

Effect of V and N Precipitation on Acicular Ferrite Formation in Sulfur-Lean Vanadium Steels

C. CAPDEVILA, C. GARCÍA-MATEO, J. CHAO, and F.G. CABALLERO

This article deals with the mechanical properties achieved in two S-lean laboratory-cast V steels with two different N content levels, as compared with commercial acicular ferrite steel. The designed heat treatments ensure an almost homogeneous microstructure consisting of acicular ferrite for N-rich and commercial steels and consisting of bainite for the N-lean steel. The results presented in this work demonstrate that, in the absence of sulfide inclusions, acicular ferrite is nucleated on V(C,N) precipitates. The mechanical tests indicate that N-rich acicular ferrite steel achieves the same toughness values as N-lean bainitic steel but with a substantial improvement in strength properties. The S-lean steels present better toughness properties than commercial acicular ferrite steel, which is consistent with the detrimental effect of inclusions on toughness.

DOI: 10.1007/s11661-008-9730-z

© The Minerals, Metals & Materials Society and ASM International 2009

I. INTRODUCTION

ACICULAR ferrite is of considerable commercial importance for plates because of its relatively high strength and toughness. Since the early 1970s, when acicular ferrite was implemented in high-strength low-alloy steel plates,^[1] much work has been done on this microstructure.^[2–10] The term “acicular ferrite” was adopted in welding and has been generalized to describe intragranularly nucleated transformation products with a relatively wide range of morphologies.^[11] The most widely accepted use of this term refers to ferrite plates nucleated intragranularly at second-phase particles. These plates usually exhibit different spatial orientations and, as a consequence, acicular ferrite microstructures are generally made up of a chaotic arrangement of plates in fine-grained interlocking morphologies that simultaneously enhance both strength and toughness.

Acicular ferrite is formed in the same temperature range as bainite (approximately 400 °C to 600 °C), by the same type of transformation mechanism.^[3] In the case of bainite, the ferrite nucleates at the austenite grain boundaries and forms packets of parallel plates with similar crystallographic orientations; acicular ferrite, on the other hand, nucleates intragranularly. The acicular ferrite transformation starts with nucleation of the primary plates at nonmetallic particles and progresses during a second stage with the formation of a new generation of ferrite plates nucleated at the austenite/primary-plate interface.^[2,5–9,12]

Acicular ferrite has been known to nucleate intragranularly at Ti-oxides dispersed in austenite grains.^[13] Although Ti₂O₃, among a number of other titanium

oxides, is believed to be the most effective nucleation site for intragranular ferrite in Ti-bearing low-carbon steels,^[14,15] some researchers have reported that TiO particles are the most effective nucleation sites for acicular ferrite.^[16–18] Recently, a new approach has been used, in an attempt to promote intragranular ferrite transformation by dispersing incoherent (MnS + V(C,N)) complex precipitates.^[19,20] In this case, the available results show that (MnS + V(C,N)) acts as a more preferential intragranular nucleation site than MnS alone, because ferrite can have any orientation relationship with respect to austenite, due to the fact that (MnS + V(C,N)) exists as an incoherent precipitate in austenite.^[21] Likewise, Madariaga *et al.*^[22] reported that an acicular ferrite microstructure is promoted instead of bainite if a suitable distribution of inclusions formed by a MnS core covered by a CuS shell is achieved. The latter exhibits good lattice matching with ferrite and poor lattice matching with austenite. On the other hand, recent studies^[23,24] have demonstrated the capability of V(C,N) precipitates to act as nucleation sites themselves for acicular ferrite, without any other inclusions.

The aim of this study was to characterize microstructural evolution during the continuous cooling of two S-lean V and N steels, as compared with commercial steel, for heavy products applications. The study is focused on both the microstructure evolution and mechanical properties. In this vein, one goal of this article is to clarify whether a N addition in a V steel is a successful strategy for promoting an acicular ferrite microstructure, from the point of view of the mechanical properties.

II. MATERIALS AND EXPERIMENTAL TECHNIQUES

The combined effect of V and N on acicular ferrite formation has been analyzed by studying the austenite decomposition in two laboratory grades: 4B and 5B, listed in Table I. A 100-kg ingot was hot rolled from a

C. CAPDEVILA, C. GARCÍA-MATEO, and F.G. CABALLERO, Tenure Scientists, and J. CHAO, Mechanical Engineer, are with the Material Research Group, Department of Physical Metallurgy, Centro Nacional de Investigaciones Metalúrgicas (CENIM-CSIC), Madrid E-28040, Spain. Contact e-mail: ccm@cenim.csic.es

Manuscript submitted June 2, 2008.

Article published online January 22, 2009

Table I. Chemical Compositions of Experimental Grades (Weight Percent)

Steel	C	Mn	V	N	Al	Si	Ti	Nb	Cu	S
4B	0.080	1.46	0.25	0.0016	0.020	0.004	0.001	—	—	0.001
5B	0.080	1.46	0.25	0.0180	0.016	0.007	0.001	—	—	0.001
12P	0.096	1.54	0.06	0.0080	<0.001	0.200	0.002	0.002	0.217	0.023

Table II. Classification Index Indicating the Length (in μm) of Inclusion According to ISO 4967 Standard

Index	A	B	C
0.5	37	17	18
1	127	77	76
1.5	261	184	176
2	436	342	320

thickness of 120 mm down to 15 mm, with a finishing rolling temperature of 1050 °C, and then air cooled down to room temperature. Additionally, an industrial heat produced by ProfilARBED-Differdange (Mittal Steel Group, Differdange, Luxembourg) for heavy beams has been used to compare the results obtained with the laboratory grades. The chemical composition is labeled as 12P and is listed in Table I.

An Adamel Lhomargy DT1000* high-resolution dila-

*DT1000(R) is a trademark of Adamel Lhomargy, Brie, France.

tometer, which is described elsewhere,^[25] has been used to determine the continuous cooling temperature (CCT) diagrams of this steel. Cylindrical dilatometric samples 2 mm in diameter and 12 mm in length were heated at 5 °C/s from room temperature up to austenitization temperatures of 1125 °C for 4B and 5B steels and 1150 °C for the 12P steel. Such differences in the austenitization temperature are selected in order to attain similar austenite grain sizes of approximately 60 μm . Subsequently, samples were gas quenched under a helium gas flow from the austenitization temperature down to room temperature at 0.5 °C/s, 1 °C/s, 2 °C/s, 4 °C/s, 6 °C/s, 10 °C/s, 25 °C/s, 50 °C/s, and 100 °C/s.

The selected heat treatments for the mechanical testing samples were performed in an adapted high-resolution furnace of an LK02 Adamel Lhomargy dilatometer described elsewhere,^[26] ensuring a homogeneous temperature in the gage length of the sample during the heat treatment.

Determination of the nonmetallic inclusion content has been carried out according to the ISO 4967 standard. In this vein, 30 fields of 0.5 μm^2 have been studied at 100 times magnification in longitudinal samples of 4B, 5B, and 12P steel. The inclusions have been grouped according to their type: sulfide (A), alumina (B), and silicate (C). A secondary index labeled 0.5, 1, 1.5, and 2 is associated with each type of inclusion. This index stands for the length and degree of the alignment of the inclusion studied. Table II lists the corresponding length of each type of inclusion with a certain index.

Table III. Thickness of Inclusion Type (in μm) According to ISO 4967 Standard

Inclusion Type	Fine	Thick
A	2 to 4	4 to 12
B	2 to 9	9 to 15
C	2 to 5	5 to 12

Likewise, the inclusions are grouped as thick or fine, according to their thicknesses, as listed in Table III.

Microtexture analysis was performed using the electron backscattered diffraction (EBSD) technique. The EBSD patterns were collected at various locations on cross sections carefully polished with colloidal silica in the final phase. The EBSD patterns were generated at an acceleration voltage of 20 kV and were collected using a CHANNEL 5 detector from HKL Technology (Danbury, CT) in a JEOL** JSM6500 field emission

**JEOL is a trademark of Japan Electron Optics Ltd., Tokyo.

gun scanning electron microscope (FEG-SEM). The indexation of the Kikuchi lines and the determination of the orientations were done with CHANNEL 5 software developed by HKL Technology. The results were represented by means of inverse pole figure maps, which give the orientation of a macroscopic direction with respect to a specific crystal direction.

Tensile specimens with a section 3 mm in diameter and a gage length of 16 mm were machined in the rolling direction of the product. Tests were performed at room temperature using a Microtest EM2/100/FR[†] testing

[†]EM/100/FR is a trademark of Microtest, Madrid, Spain.

machine fitted with a 100-kN load cell. A crosshead speed of $8.3 \times 10^{-3} \text{ mm s}^{-1}$ was used in all the experiments. From the engineering stress-strain curves, 0.2 pct yield stress (YS), ultimate tensile strength (UTS), uniform elongation, (UE) and total elongation (TE) were obtained. Strain hardening was characterized by analyzing the incremental strain-hardening exponent (n_i), defined as $n_i = d(\ln \sigma_p)/d(\ln \epsilon_p)$, in the plastic regime of the true stress-strain curves.

Subsized V-notch (2 mm in depth) Charpy specimens $10 \times 2.5 \times 55 \text{ mm}^3$ in size were machined in the longitudinal transverse direction, according to the E399 Crack Plane Orientation Code, for rectangular sections.^[27] The capacity of the Charpy pendulum was

147 J and the hammer velocity in the instant of impact was approximately 5.4 m s^{-1} . In order to provide the ductile-brittle transition (DBT) temperature, Charpy (K_V) tests were carried out at temperatures ranging from room temperature to $-196 \text{ }^\circ\text{C}$. The DBT temperatures were determined for an impact energy equal to one-half of the difference between the respective minimum- and maximum-impact energies ($0.5 \Delta K_V$).

III. RESULTS

A. Nonmetallic Inclusions Analysis

As was reported in Section I, nonmetallic inclusions can act as nucleation sites for acicular ferrite. Hence, characterization of the nonmetallic inclusion content is of vital importance in this study. The determination of the nonmetallic inclusion content in the as-received condition of steels has been carried out according to the ISO 4967 standard. Table IV lists the results obtained for A-, B-, and C-type inclusions. It is clear that 12P steel has a larger volume of inclusions, mainly of the sulfide type, which is clearly consistent with the chemical composition listed in Table I.

B. Microstructural Analysis

The CCT diagrams of the steels listed in Table I are presented in Figure 1. Figure 2 shows the microstructure obtained in the three steels studied after continuous cooling at $6 \text{ }^\circ\text{C/s}$. This cooling rate corresponds to the maximum amount of acicular ferrite formed by continuous cooling in 5B and 12P steels. It is observed that grain-boundary nucleation sites are saturated by the ferrite formed during continuous cooling before the acicular ferrite transformation. Hence, acicular ferrite is formed intragranularly by transformation of the

remaining austenite. On the other hand, bainite is formed instead of acicular ferrite in the 4B steel. The metallographic examination of microstructures obtained at different cooling rates is summarized in Table V. It is clear from Figure 1 and Table V that the continuously cooled microstructures are a mixture of proeutectoid ferrite, pearlite, bainite, acicular ferrite, and martensite in different proportions, depending on the cooling rate.

With the aim of obtaining a homogeneous microstructure of either acicular ferrite or bainite, a two-step cooling was designed in accordance with the CCT diagrams shown in Figure 1. These heat treatments are summarized in Table VI. Two cooling paths (routes 1 and 2 in Figure 1) can be distinguished in line with the temperature at which the cooling rate changes from $50 \text{ }^\circ\text{C/s}$ to $2 \text{ }^\circ\text{C/s}$ (hereafter called the temperature change (TC)). A TC of $630 \text{ }^\circ\text{C}$ (route 1) was considered, in order to maintain the steel inside the acicular ferrite

Table IV. Classification and Number of Inclusions Detected in 30 Fields of View for 4B, 5B, and 12P Steels

Inclusion Type	Index		4B	5B	12P
A	0.5	fine	0	0	0
		thick	1	0	3
	1	fine	0	0	0
		thick	2	0	8
	1.5	fine	0	0	0
		thick	0	0	10
2	fine	0	0	0	
	thick	0	0	1	
B	0.5	fine	0	3	1
		thick	1	0	0
	1	fine	0	5	1
1.5	fine	1	1	1	
	thick	0	0	0	
	thick	0	0	0	
C	0.5	fine	0	0	0
		thick	0	0	0
	1	fine	0	0	0
		thick	1	0	1
1.5	fine	0	0	0	
	thick	0	0	0	

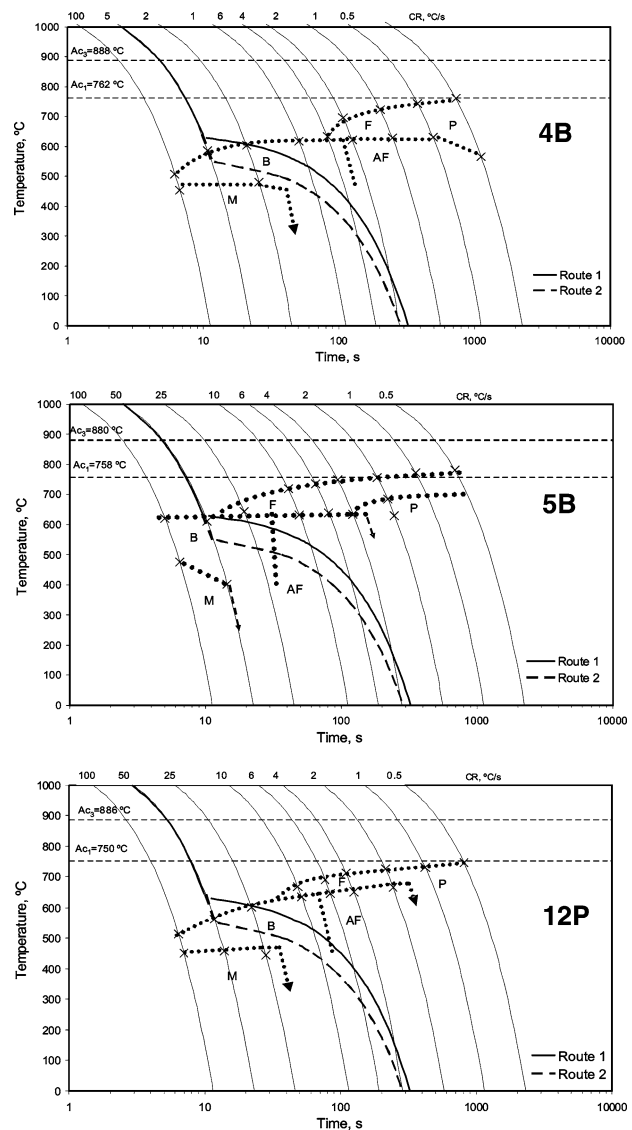
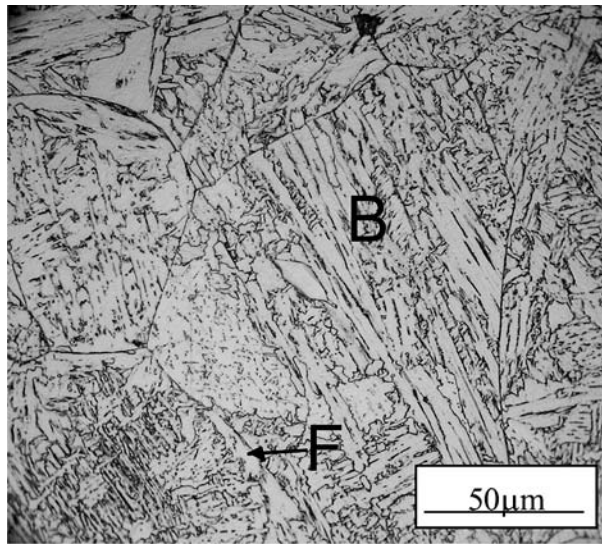
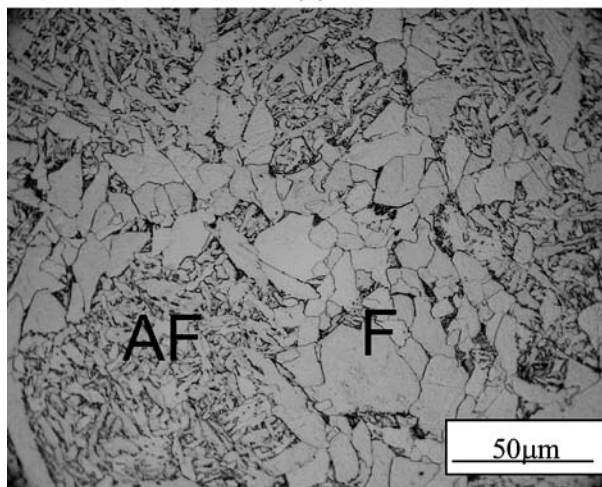


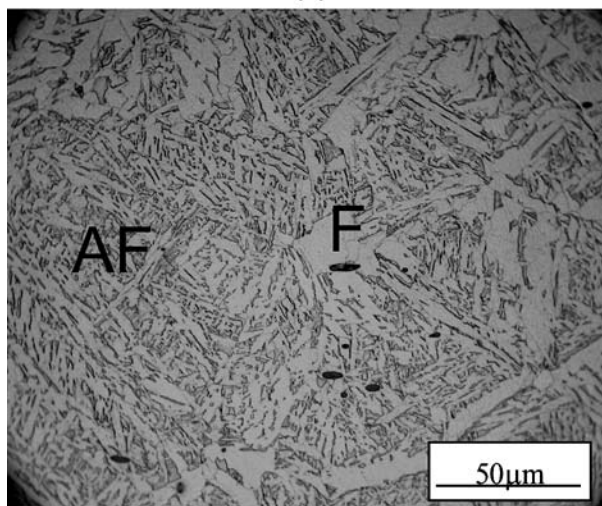
Fig. 1—CCT diagrams of studied steels. routes 1 and 2 are defined according to Table V. (F stands for ferrite, P for pearlite, AF for acicular ferrite, B for bainite, and M for martensite.)



(a)



(b)



(c)

Fig. 2—Optical micrographs of developed microstructures after continuous cooling at 6 °C/s in (a) 4B, (b) 5B, and (c) 12P steels. (F stands for ferrite, B for bainite, and AF for acicular ferrite.)

Table V. Microstructure Identification Results

Cooling Rate (°C/s)	Microstructure*		
	4B	5B	12P
0.5	F/AF > P	F > P	F > P
1	F/AF > P↓↓	F > P	F > P↓
2	AF > F	F > AF > P	AF > F > P↓↓
4	B > F	F/AF	AF > F
6	B > F↓	AF > F	AF > F
10	B	AF > F↓	B > F
25	B/M	F > B > AF	B > M
50	M > B	M > B	M > B
100	M > B↓	M > B↓	M > B↓

*F = ferrite, P = pearlite, B = bainite, AF = acicular ferrite, and M = martensite.

Table VI. Heat Treatments Applied and Microstructure Obtained

Steel	Cooling Path	Cooling Rate (°C/s)	Microstructure
4B	route 1	$T_{\gamma}^{50^{\circ}\text{C/s}} \rightarrow 630^{\circ}\text{C}^{2^{\circ}\text{C/s}} \rightarrow \text{RT}$	B
4B	route 2	$T_{\gamma}^{50^{\circ}\text{C/s}} \rightarrow 550^{\circ}\text{C}^{2^{\circ}\text{C/s}} \rightarrow \text{RT}$	B
5B	route 1	$T_{\gamma}^{50^{\circ}\text{C/s}} \rightarrow 630^{\circ}\text{C}^{2^{\circ}\text{C/s}} \rightarrow \text{RT}$	AF + B↓↓
5B	route 2	$T_{\gamma}^{50^{\circ}\text{C/s}} \rightarrow 550^{\circ}\text{C}^{2^{\circ}\text{C/s}} \rightarrow \text{RT}$	AF + B↓
12P	route 1	$T_{\gamma}^{50^{\circ}\text{C/s}} \rightarrow 630^{\circ}\text{C}^{2^{\circ}\text{C/s}} \rightarrow \text{RT}$	B + AF
12P	route 2	$T_{\gamma}^{50^{\circ}\text{C/s}} \rightarrow 550^{\circ}\text{C}^{2^{\circ}\text{C/s}} \rightarrow \text{RT}$	B + AF

field as much as possible, but with a relative risk of some proeutectoid ferrite formation. A second TC of 550 °C (route 2) was selected, in order to achieve a fine acicular ferrite microstructure. Likewise, proeutectoid ferrite is avoided. Figure 3 shows the microstructure obtained in the two-step cooling for 5B, 4B, and 12P steels. Quasihomogeneous microstructures of acicular ferrite and bainite in 5B and 4B steels, respectively, were obtained. A mixture of acicular ferrite and bainite was observed in 12P steel.

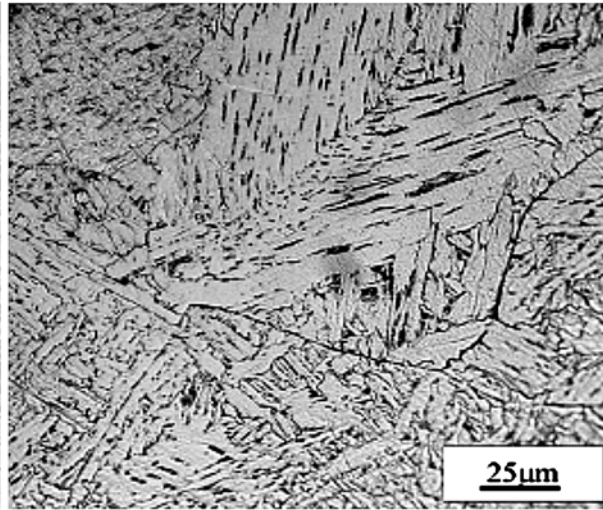
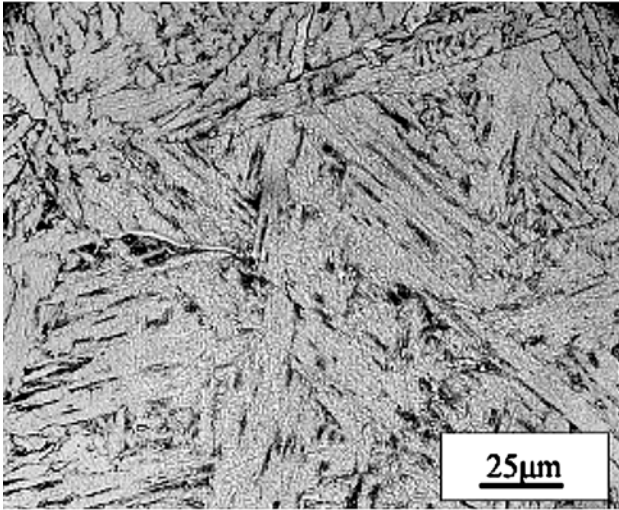
C. Tensile Testing Results

Results that correspond to the tensile tests are presented in Table VII. The results presented here correspond to the average of at least two tests.

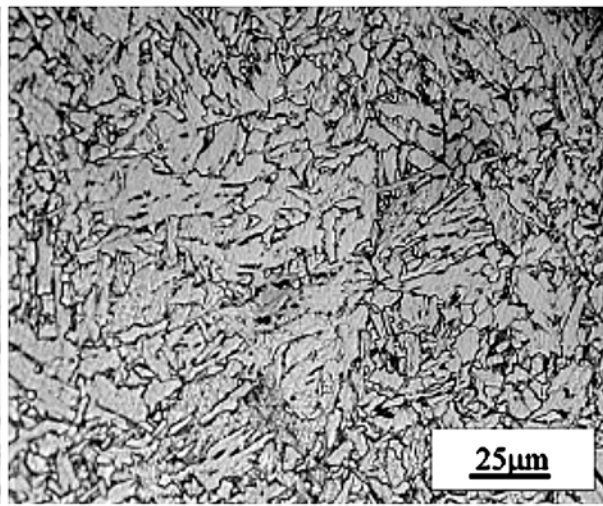
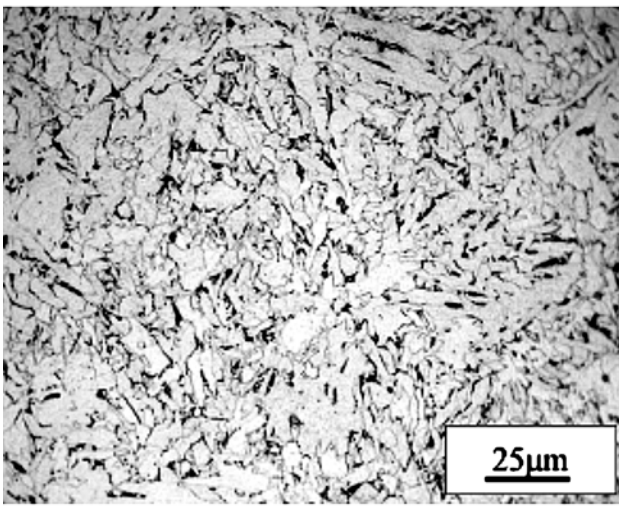
Figure 4 shows the evolution of the instantaneous strain-hardening coefficient (n_i) for the two values of the TC temperature studied. The value of n_i indicates the hardening rate of the material. The relative maximum in the curves indicates the true strain at which the maximum work hardening is recorded. The straight line in the graphs corresponds to the instability criterion, *i.e.*, the loci of points at which $n = \epsilon_{ii}$; it is an indication of the point at which necking starts. An ideal plastic material in which no strain hardening occurs would become unstable in tension and would begin to neck just as soon as yielding took place.

TC = 630 °C

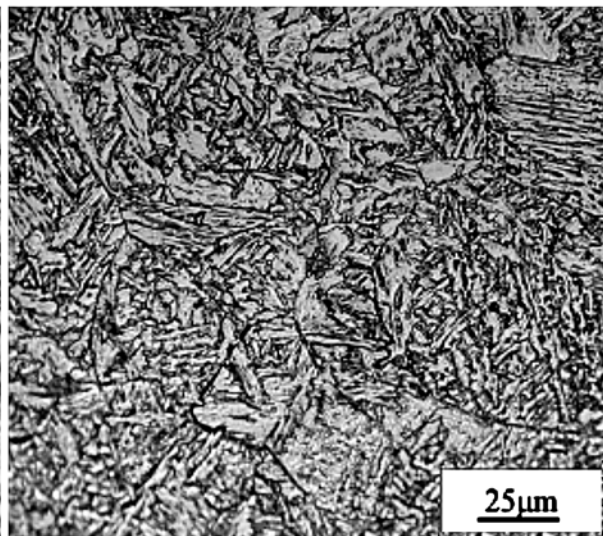
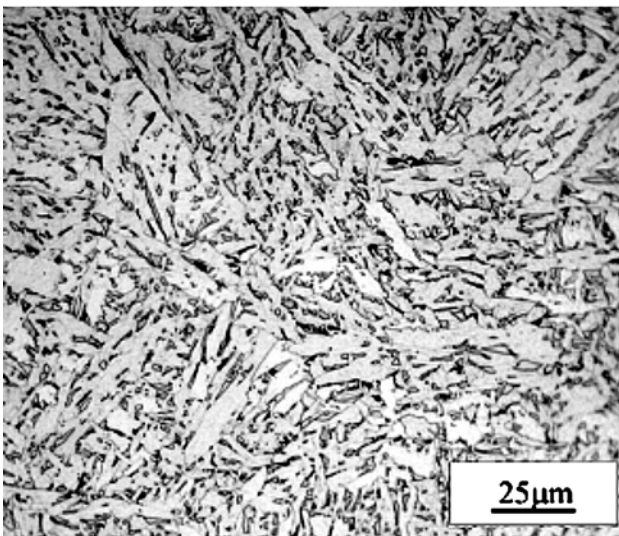
TC = 550 °C



(a)



(b)



(c)

Fig. 3—Optical micrographs of the developed microstructure after two-step cooling at TC temperatures of 630 °C and 550 °C in (a) 4B, (b) 5B, and (c) 12P steels.

Table VII. Summary of Mechanical Properties (Average of Two Tests)

Steel	TC (°C)	YS (MPa)	UTS (MPa)	UTS/YS (MPa)	UE (Pct)	TE (Pct)	RA* (Pct)
4B	630	462	572	1.23	5.5	25	74
	550	522	625	1.20	3.2	22	79
5B	630	515	633	1.24	6.0	26	75
	550	530	659	1.23	6.3	25	78
12P	630	441	612	1.39	8.3	21	74
	550	495	634	1.28	5.8	19	75

*RA = reduction in area.

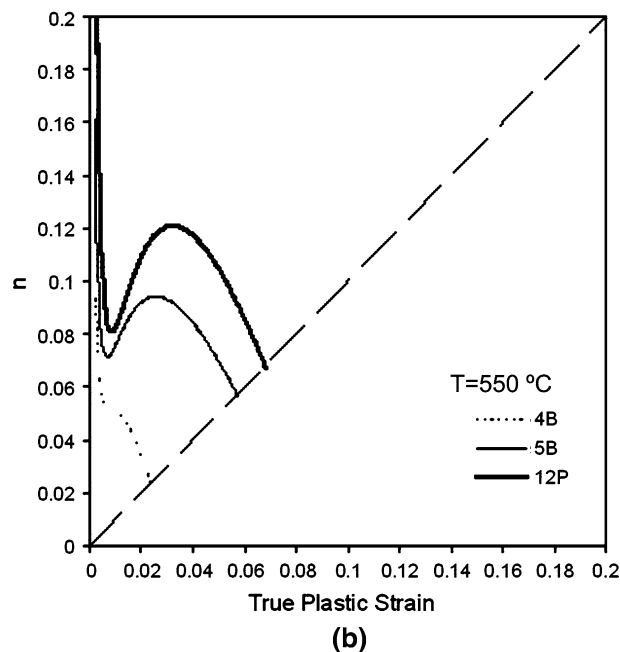
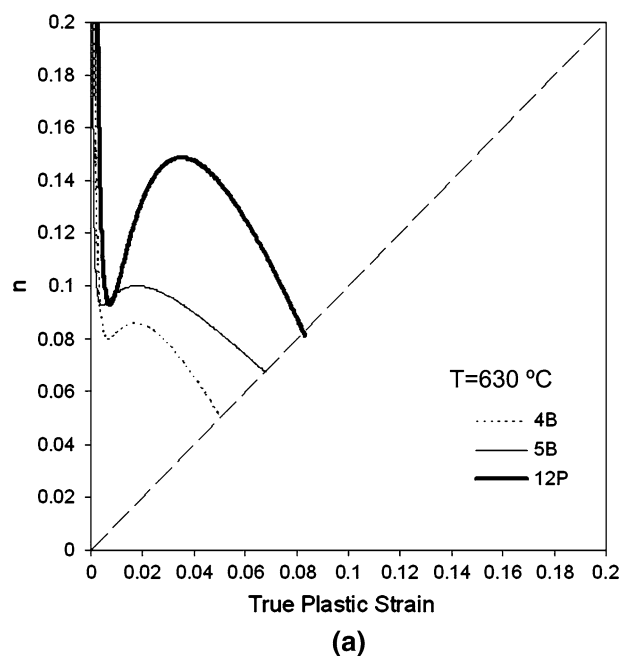


Fig. 4—Work-hardening coefficient for 5B, 4B, and 12P steels with TC = (a) 630 °C and (b) 550 °C.

D. EBSD Measurements

Figure 5 shows the quality image, orientation-color maps, and high-angle boundary maps measured by EBSD for 4B and 5B steels at a TC temperature of 630 °C. The crystallographic packet size could be defined as the mean distance (d) between high-angle boundaries (>15 deg). The value of d has been determined from the lines traced on the high-angle boundary maps of 4B and 5B steels, such as the one shown in Figure 5(c). From each scanned zone, two lines were traced from one set of corners to the opposite set of corners in the area, and a third line was traced parallel to the minor side of the rectangular area such that the three lines intersect at one point. The lowest value of d obtained corresponds to the 5B steel (3.5 μm). The 4B steel presents a larger value of $d = 10.0 \mu\text{m}$.

E. Charpy Impact Tests

Figures 6(a) and (b) show the Charpy impact energy as a function of the test temperature for the three steels at TC temperatures of 630 °C and of 550 °C, respectively. A quick view of this figure reveals the same absorbed-energy values in Charpy tests performed at $-196 \text{ }^\circ\text{C}$ for the three steels studied (a value of 0.48 J). However, the three steels studied exhibit different behaviors at the DBT temperature and at the absorbed energy of the upper shelf.

F. Fractographic Analysis

The fracture aspect of 5B steel (TC temperature of 630 °C) tested at $-196 \text{ }^\circ\text{C}$ is shown in Figure 7. The initiation sites were located 500 μm from the notch tip. No appreciable ductile tearing before cleavage fracture was observed; only cleavage was observed, as would be expected when the impact energy is nearly zero. The initiation sites were identified by tracing the river lines to an origin. The initiation site itself was featureless.

Figure 8 shows the fracture surface of the 5B specimen (TC temperature of 630 °C) tested at $-80 \text{ }^\circ\text{C}$. The upper part of the fracture surface shows a nearly ductile appearance. A central thin band can be seen in which plane strain conditions prevail, *i.e.*, relatively high-stress triaxiality conditions. In this band, the fracture occurs *via* the nucleation, growth, and coalescence of microvoids. At both sides of the band, the fracture occurs with relatively low-stress triaxiality conditions, *i.e.*, without

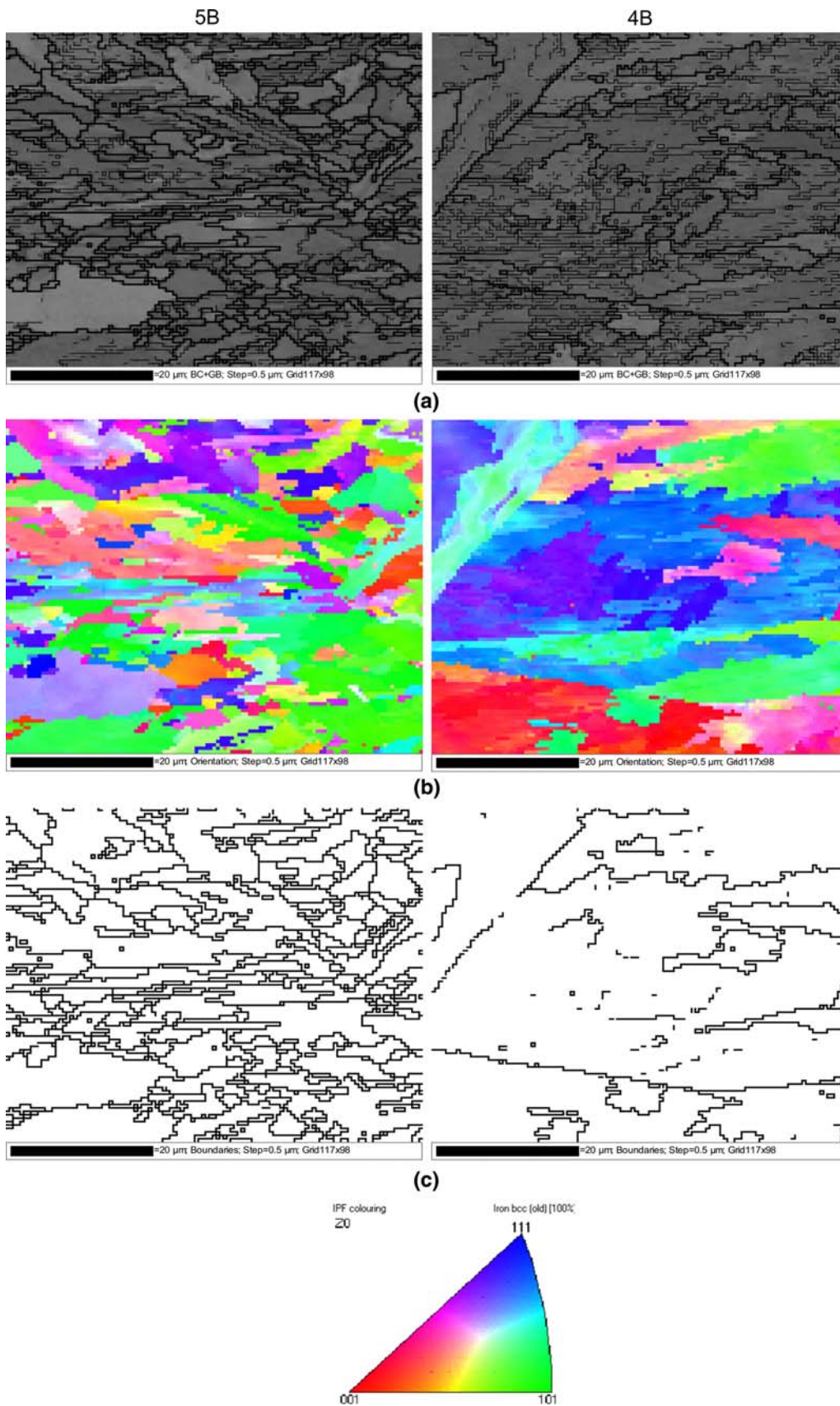


Fig. 5—EBSD analysis of 5B and 4B steels: (a) quality images, (b) orientation image map, and (c) high-angle boundary maps (misorientations > 15 deg).

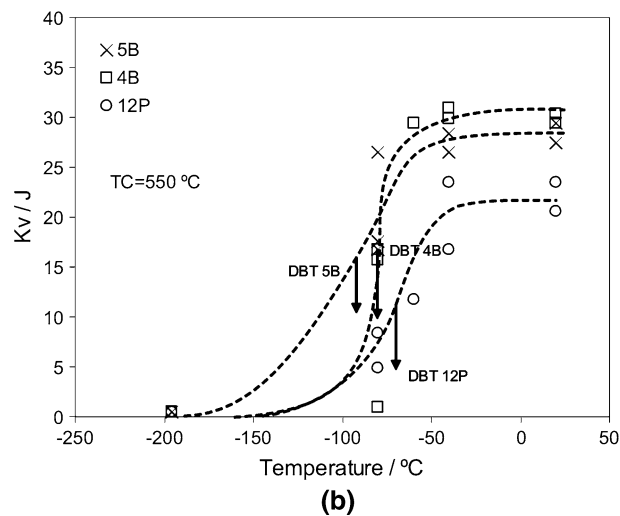
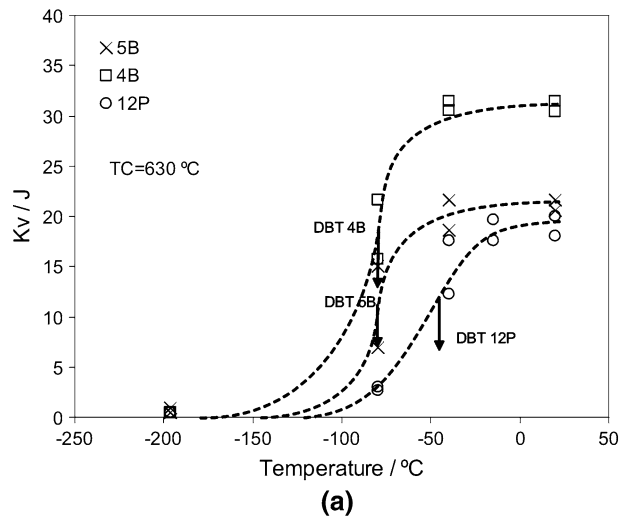


Fig. 6—DBT curve in 4B, 5B, and 12P steels for TC = (a) 630 °C and (b) 550 °C. Arrows stand for DBT temperature, which corresponds to $0.5 \Delta K_{Ic}$.

plane stress conditions. In these zones, the fracture occurs by ductile shear. The lower part of the fracture surface shows a brittle aspect in which full plane strain conditions are reached as the crack advances. The fracture in this zone occurs by cleavage and the initiation is located in the squared area; this shows that the fracture begins in a grain boundary.

The fracture surface of the 4B sample tested at -80 °C (TC temperature of 630 °C) is shown in Figure 9. As for the previous case of the 5B steel, fractographic analysis reveals that cleavage fracture initiates at a grain boundary. In none of the cleavage fracture surfaces were analyzed particles found at the fracture origin. Similar conclusions could be drawn from the fractographic analysis of the Charpy specimens obtained from the samples treated with a TC = 550 °C.

Figures 10 and 11 show scanning electron microscopy images of the fracture surfaces of the 4B and 5B specimens (TC temperature of 550 °C) tested at -80 °C. The fracture mode is similar to that described earlier for the TC = 630 °C material. A closer view of the cleavage

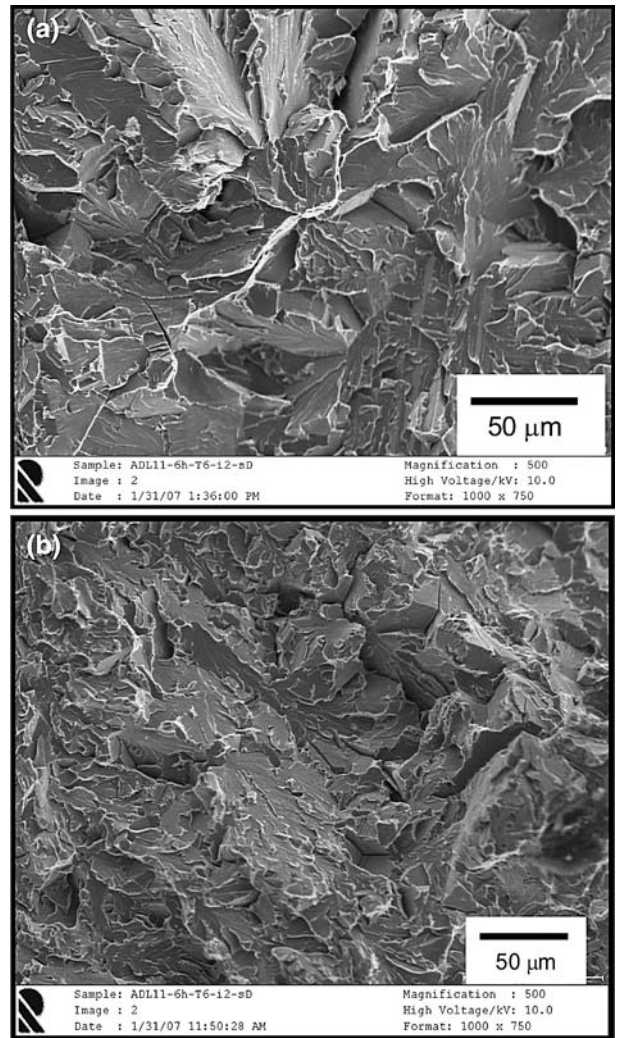


Fig. 7—Fractographic analysis of (a) 4B and (b) 5B steels tested at -196 °C (TC = 630 °C).

initiation zone shows again that cleavage nucleates at a grain boundary.

Figure 12 shows the fracture aspect of the 12P specimen (TC of 630 °C) tested at -80 °C. The fracture takes place first by ductile tearing approximately $60 \mu\text{m}$ from the notch tip and then by cleavage. Different from 4B and 5B steels, the cleavage fracture initiation for 12P steel is associated with precipitates nucleated near MnS inclusions. It is also worth noting that the inclusions themselves do not directly contribute to the initiation of the cleavage fracture, but enhance the nucleation stage in neighboring particles. The drop in the TC temperature to 550 °C does not affect the nucleation of cleavage fracture in the 12P steel; instead, this is associated with an inclusion, as shown in Figure 13.

IV. DISCUSSION

The inclusion analysis results listed in Table IV revealed that 4B and 5B steels are almost free of inclusions; a significant amount of sulfides, however, is

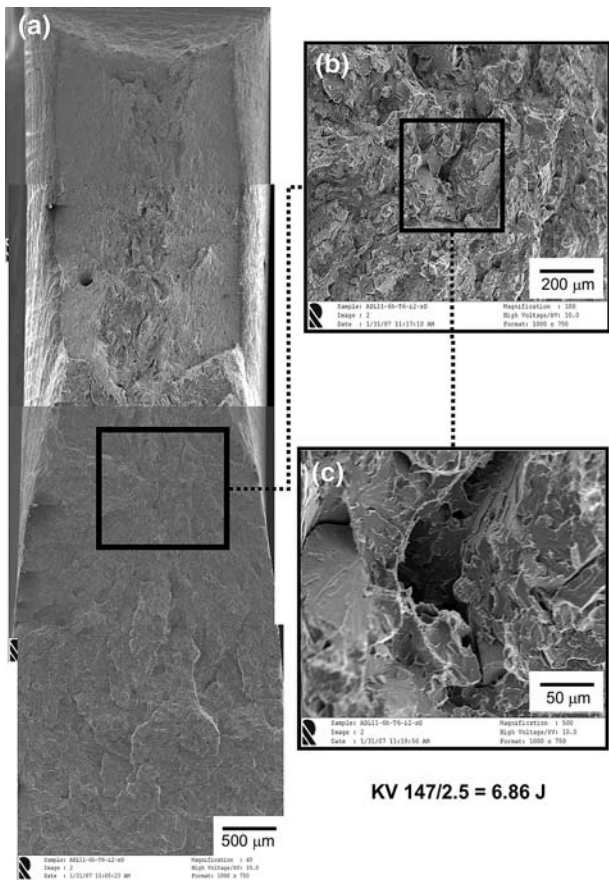


Fig. 8—Fractographic analysis of 5B steel sample (TC = 630 °C) tested at -80 °C.

present in 12P steel. Additionally, microstructural analysis revealed that acicular ferrite is the main phase present in the microstructure, in both 5B and 12P steels. Although it is sensible to assume that acicular ferrite nucleates on the sulfides in 12P steel, this assumption is no longer valid for 5B steels, according to the results listed in Table VI. It is clear that acicular ferrite nucleates in different places in 5B and 12P steels.

Figure 14 shows the nucleation sites of acicular ferrite for both 5B (Figure 14(a)) and 12P (Figure 14(b)) steels. The FEG-SEM micrographs and energy-dispersive X-ray spectra shown revealed that, while V(C,N) precipitation takes place as isolated precipitates in 5B steels, a process that involves a coupled sulfide + V(C,N) complex system is formed in 12P steel.

The results mentioned here could explain the presence of acicular ferrite in 5B and 12P steels. However, the reason that acicular ferrite is the major phase in 5B steel is still unclear; it is not present in 4B steel, however, which presents the same C and V content. In order to clarify this point, Figure 15 shows the evolution of MnS and V(C,N), along with ferrite and austenite phases, in all the steels calculated by means of MTDATA[‡] using a

[‡]MTDATA is a trademark of National Physical Laboratory (NPL), Teddington, UK.

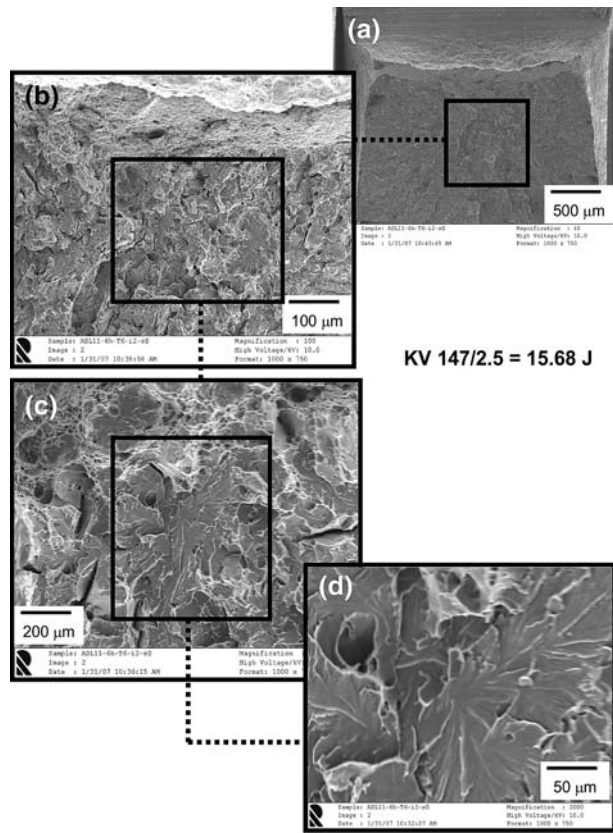


Fig. 9—Fractographic analysis of 4B steel sample (TC = 630 °C) tested at -80 °C.

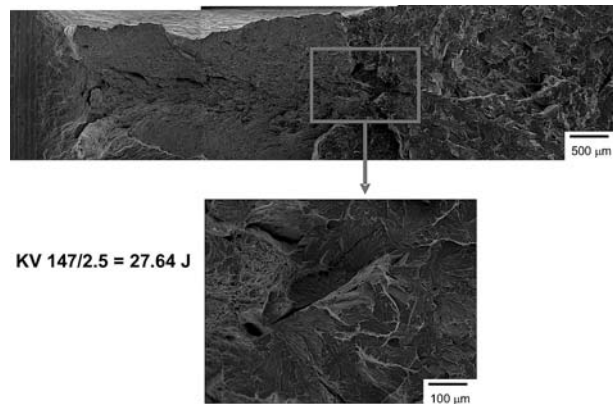


Fig. 10—Fractographic analysis of 4B steel sample (TC = 550 °C) tested at -80 °C.

standard scientific group thermodata Europe (SGTE) database. It is clear from this figure that a representative fraction of V precipitation takes place within the austenite field in 5B steel. However, that is not the case for 4B steel, in which most of the precipitation takes place in the ferrite field. This leads to a higher number of pre-existent precipitates prior to the austenite decomposition in 5B steel, as compared to 4B steel, which

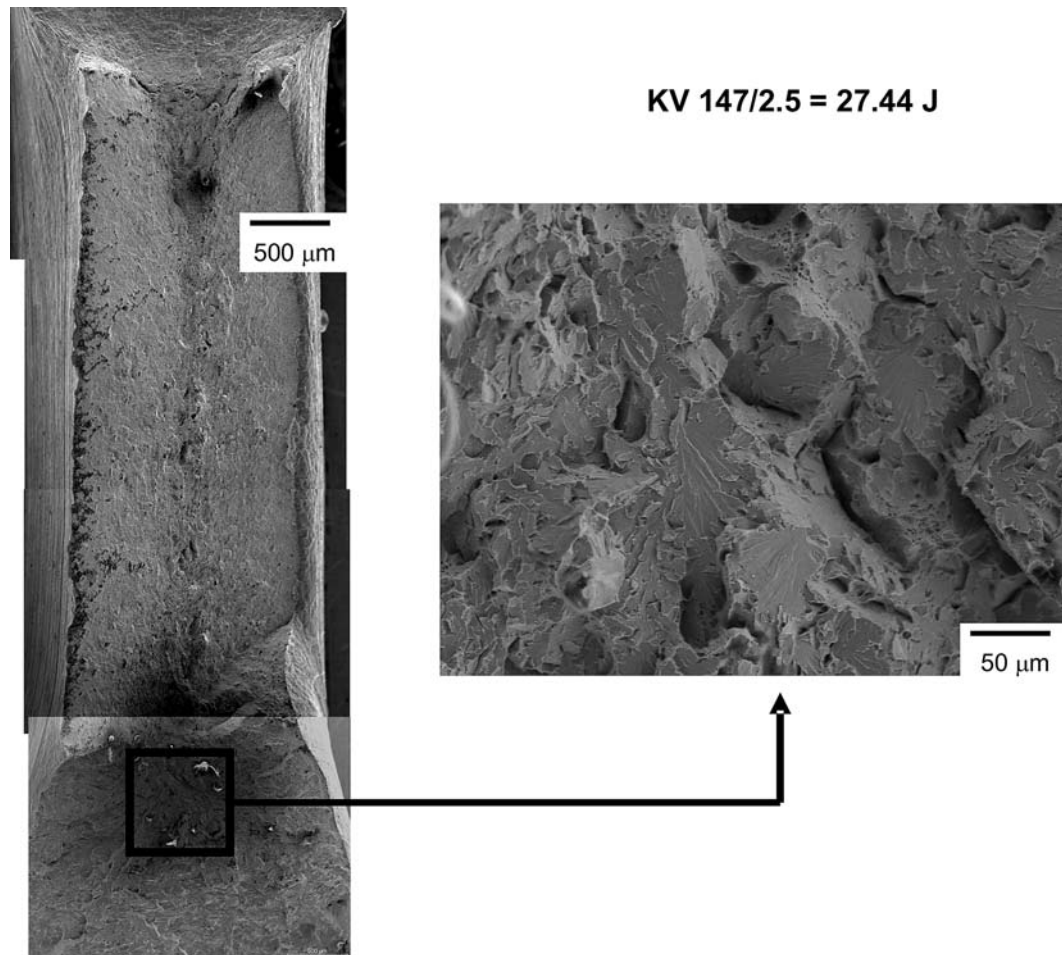


Fig. 11—Fractographic analysis of 5B steel sample (TC = 550 °C) tested at –80 °C.

explains the increase in the acicular ferrite volume fraction.^[23,24]

Moreover, it is seen in Figure 15 that the dissolution of V(C,N) in 5B steel is predicted to occur above 1200 °C. It is worth noting that the austenitization temperature of 5B steel was 1125 °C, which suggests that not all of the V(C,N) precipitates formed during processing of the steel have been dissolved. Because the finishing rolling temperature is 1050 °C, it is likely that the precipitation of V took place intragranularly in unrecrystallized austenite. This could explain the intragranular distribution of V(C,N) in 5B steel. On the contrary, the lack of N in 4B steel will shift the composition of V precipitates from V(C,N) to almost pure VC, which presents a significantly lower dissolution temperature (approximately 950 °C).^[23,24] Therefore, it is likely that most of the V precipitates in 4B are dissolved during austenitization treatments before CCT and the two-step cooling cycles; hence, the subsequent V precipitation during cooling takes place on austenite grain boundaries, which are not effective for acicular ferrite nucleation.

These differences in V precipitation in 4B and 5B steels can explain the microstructural differences observed in the CCT diagrams and the two-step cooling cycles. In this vein, although some islands of acicular

ferrite are detected in 4B steel, it is not the major decomposition product obtained at any of the cooling rates tested. The addition of N (5B steel) results in the combination of V and N optimal for inducing the formation of acicular ferrite, even in the absence of S, as the results presented in the corresponding CCT diagrams clearly show. The importance of sulfide inclusions in the acicular ferrite formation is revealed in a comparison of the results obtained in 12P and 4B steels, as shown in Figures 3(c) and (a), respectively. In 12P steel, the amount of S and Cu is high enough to ensure the formation of sulfides that will promote the formation of acicular ferrite, as shown in Figure 14(b).

On the other hand, the analysis of microstructures obtained in the two-step cooling process indicates that, although no variation in the type of microstructure is obtained, a microstructural refinement is observed as the TC decreases. In 5B steel (Figure 3(b)), an increase in the bainite volume fraction is also noticeable as the TC drops down to 550 °C, which is consistent with the CCT diagram reported in Figure 1. In this diagram, it is observed that the cooling from 630 °C occurs mainly in the acicular ferrite field of the diagram; however, the first stages of cooling from 550 °C occur in the bainitic field. Because this transformation is fairly rapid in this material, it is likely that a certain amount of the

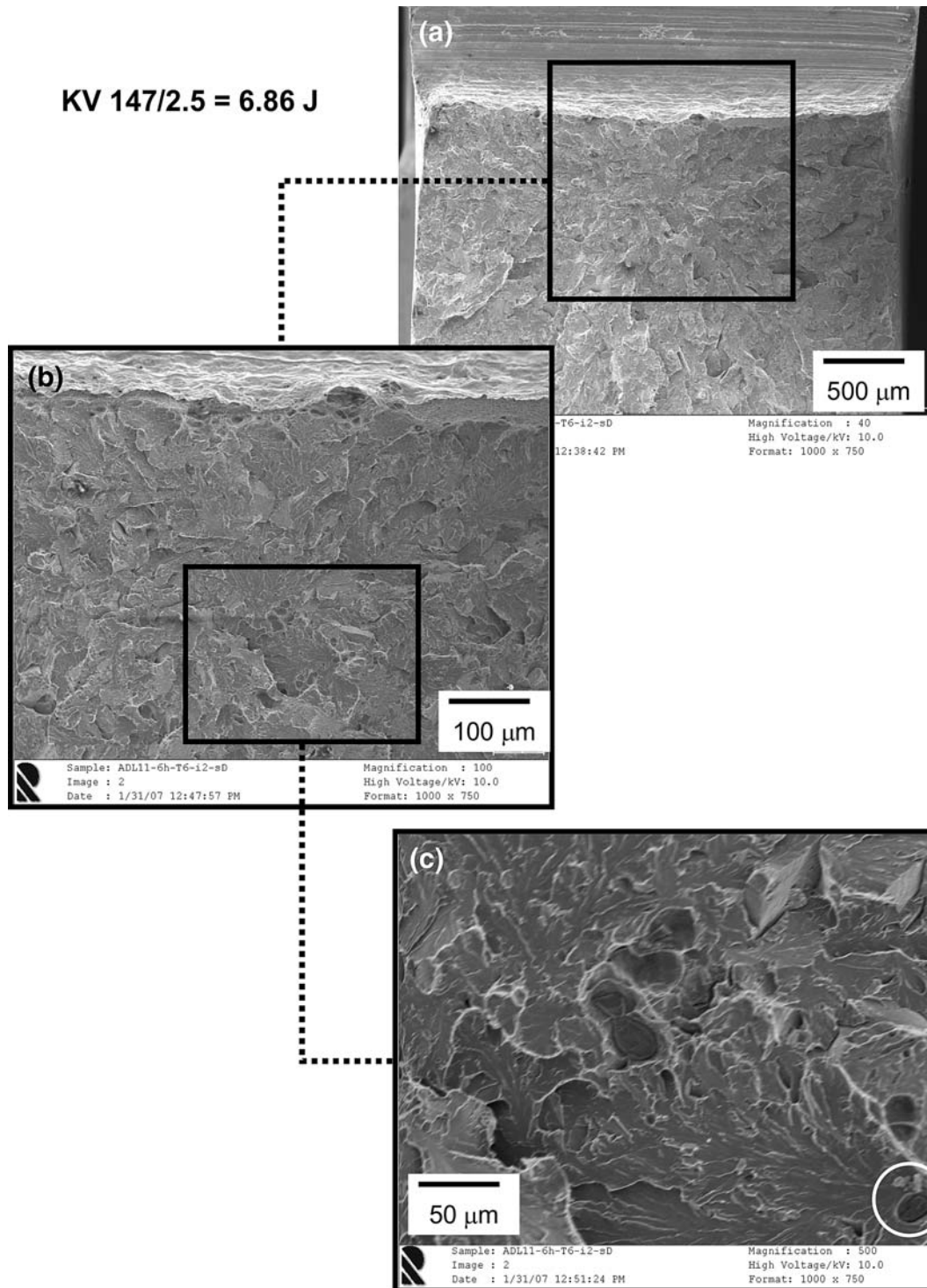


Fig. 12—Fractographic analysis of 12P steel sample (TC = 630 °C) tested at -80 °C.

microstructure would transform before the acicular ferrite field is reached. These bainitic regions are the ones with parallel ferrite laths in the microstructure, as shown in Figure 3(b).

The bainitic or acicular ferrite microstructures obtained after the two-step cooling do not significantly affect the strength of the properties listed in Table VII. In general, slightly higher YS and UTS values are

observed in 5B steel as compared to 4B and 12P steels, for both TC temperatures tested. Moreover, the YS and UTS values increase as the TC temperature drops because of the refinement of the microstructure. However, this increase in strength does not have a counterpart in the decrease in TE values, which are very similar among the three steels studied, regardless of the TC. As for UE, a decrease of approximately 40 pct was

KV 147/2.5 = 17.44 J

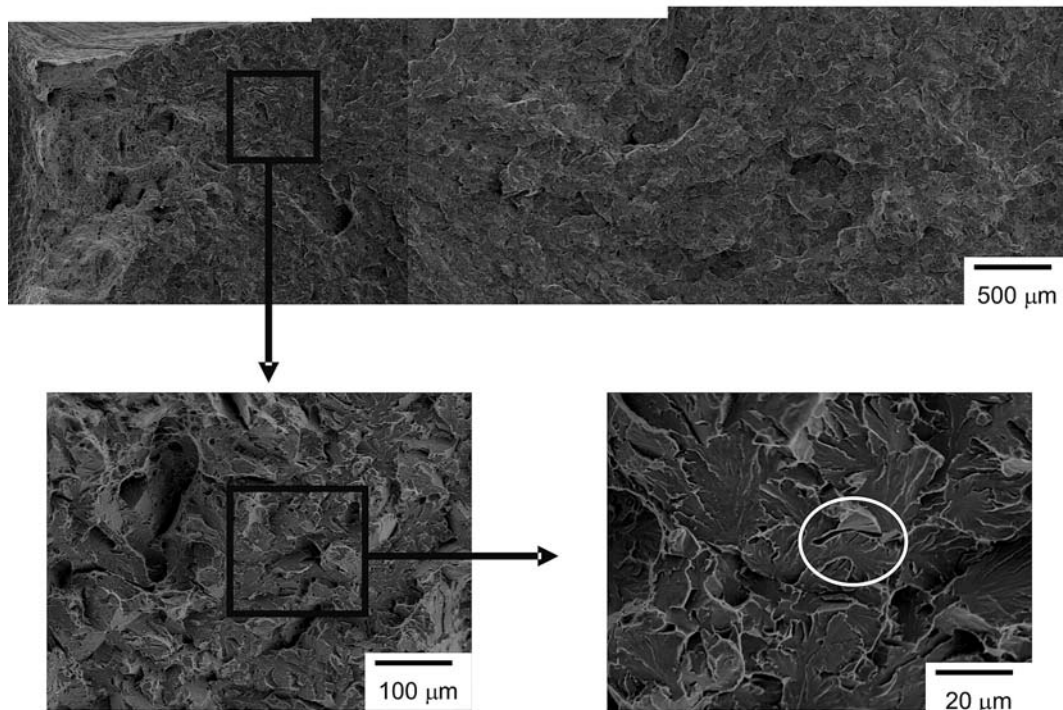


Fig. 13—Fractographic analysis of 12P steel sample (TC = 550 °C) tested at –80 °C. Encircled is the inclusion at which crack initiates.

observed in the 4B and 12P steels, whereas no marked changes were detected for the 5B steel. These observations indicate the detrimental effect of a decreasing TC on the plastic behavior of 4B and 12P steels. However, 5B steel is able to keep the same levels of ductility with an increment in strength.

In relation to the work-hardening behavior, a decrease in the values of n_i with decreasing TC temperatures have been recorded for the three steels studied (Figure 4), which is consistent with the values of the UTS/YS ratio listed in Table VII. It is obvious from Figure 4 that 12P steel hardens on a larger scale than 4B and 5B steels. Moreover, the strain at which a maximum of n_i is recorded ($\epsilon_{n\text{-max}}$) is similar for 4B and 5B steels and is significantly lower than that for 12P steel. The drop in TC from 630 °C to 550 °C does not significantly affect this trend for 5B and 12P steels, *i.e.*, the value of $\epsilon_{n\text{-max}}$ for 12P steel is still higher than that for 5B steel, but to a lower extent than in the previous case. The most remarkable difference is produced in the 4B steel, for which $\epsilon_{n\text{-max}}$ is recorded, because a continuous decrease in hardening is observed. Regarding the 5B steel, there is a shift in ϵ_u to higher strain values, which indicates that the microstructure obtained after a TC of 630 °C allows the material to deform uniformly (keeping the dimensionality ratio) to a larger extent than the microstructure obtained with a TC of 550 °C.

Therefore, from the analysis of the results presented here, it could be concluded that $\epsilon_{n\text{-max}}$ is slightly higher in the acicular ferrite (5B) steel than in the bainitic (4B) steel; this means that the higher misorientation between the ferrite plates (as could be concluded from Figure 5) and the higher volume of V(C,N) precipitates leads to

higher values of YS and UTS and the maintenance of similar levels of TE in the 5B as compared to the 4B steel, *i.e.*, the 5B steel has strength values higher than those observed in the bainitic steel while maintaining the same ductility.

As a general comment on toughness behavior, it can be concluded from Figure 6 that 12P steel presents a poorer toughness behavior than 4B and 5B steels, which is consistent with the higher amount of sulfide inclusion in this steel. Likewise, different behaviors corresponding with the TC temperature are observed for the 4B and 5B steels, in both the transition temperature and the upper-shelf regions of the DBT curves shown in Figure 6; these deserve an explanation.

For the upper-shelf results, a comparison of Figures 6(a) and (b) reveals that 4B steel presents the highest value of energy in the upper shelf at both TC temperatures considered. As is well known, in this region of the DBT curve, the fracture occurs through the nucleation, growth, and coalescence of microvoids. The fracture event takes place at the point at which a critical plastic strain is reached on a microstructure-related critical distance.^[28] The critical strain is a function of the microstructure (the morphology, size, and distribution of the inclusions) and the stress triaxiality state.^[29,30] Moreover, for similar microstructural states, the energy in the upper-shelf region decreases with an increase in the strength level of the steel.^[31] Therefore, the higher absorbed-energy value recorded for 4B steel can be attributed to the lower YS of this steel (Table VII), because both 4B and 5B steels have a similar inclusionary state (Table VI). The similar absorbed energies in the upper-shelf region observed for 4B and 5B steels at a

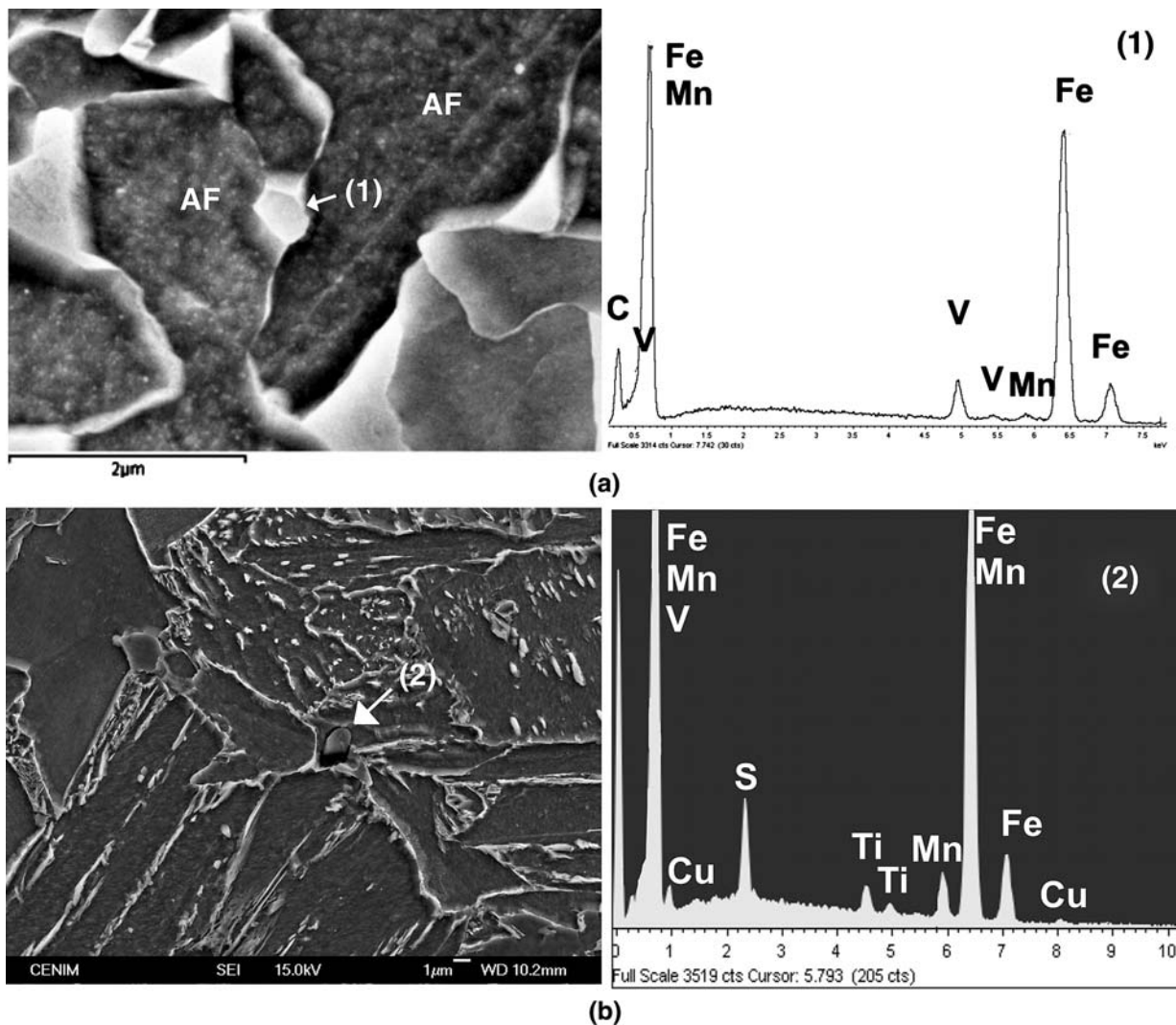


Fig. 14—Acicular ferrite nucleation in (a) V(C,N) in 5B steel and (b) (Mn,Cu)S + (Ti,V)(C,N) in 12P steel.

TC temperature of 550 °C are fully consistent with this reasoning. However, a comparison of the absorbed energy of 12P steel with the absorbed energies of 4B and 5B steels reveals that the expected increase in the absorbed energy for 12P steel (because 12P presents the lowest YS values) is offset by the higher inclusion content of this steel, regardless of the TC temperature studied.

On the other hand, the upper-shelf energy of 5B steel presents an unexpected behavior. The value of the absorbed energy matches that obtained for 4B steel at a TC temperature of 550 °C, but presents as significantly lower for the TC temperature of 630 °C (lower YS value). This behavior could be related to cementite precipitation, which strongly depends on the TC temperature. In this vein, coarse cementite precipitates can be disclosed in the microstructure of 5B steel at a TC temperature of 630 °C, as can be seen in the left side of the picture in Figure 3(b); much finer precipitates, on the other hand, are formed during cooling after a TC of 550 °C (the right side of the picture in Figure 3(b)).

The value of $0.5 \Delta K_{Ic}$ in Figure 6 allows us to determine the DBT temperatures of 4B, 5B, and 12P steels. In this vein, values of -80 °C, -80 °C, and -45 °C for a TC of 630 °C (Figure 6(a)), and -80 °C, -90 °C, and -70 °C for a TC of 550 °C (Figure 6(b)) were obtained in 4B, 5B, and 12P steels, respectively. In the DBT region, the fracture occurs first through ductile tearing and then by cleavage, with the absorbed energy related to the proportion of ductile fracture. Assuming that the formation of dislocation pileup is the mechanism necessary for stress intensification and the triggering of the cleavage fracture in a particle or grain boundary, the transition temperature would decrease as the grain size decreases.^[32] In order to be more precise, it is better to discuss the results on the basis of an “effective grain size,” which is defined as the region in which the crack propagates nearly in a straight line; this corresponds to the continuous set of ferrite plates with a crystallographic misorientation lower than 15 deg (crystallographic packet).^[33–35] This trend has been experimentally validated previously,^[33] but it does not appear

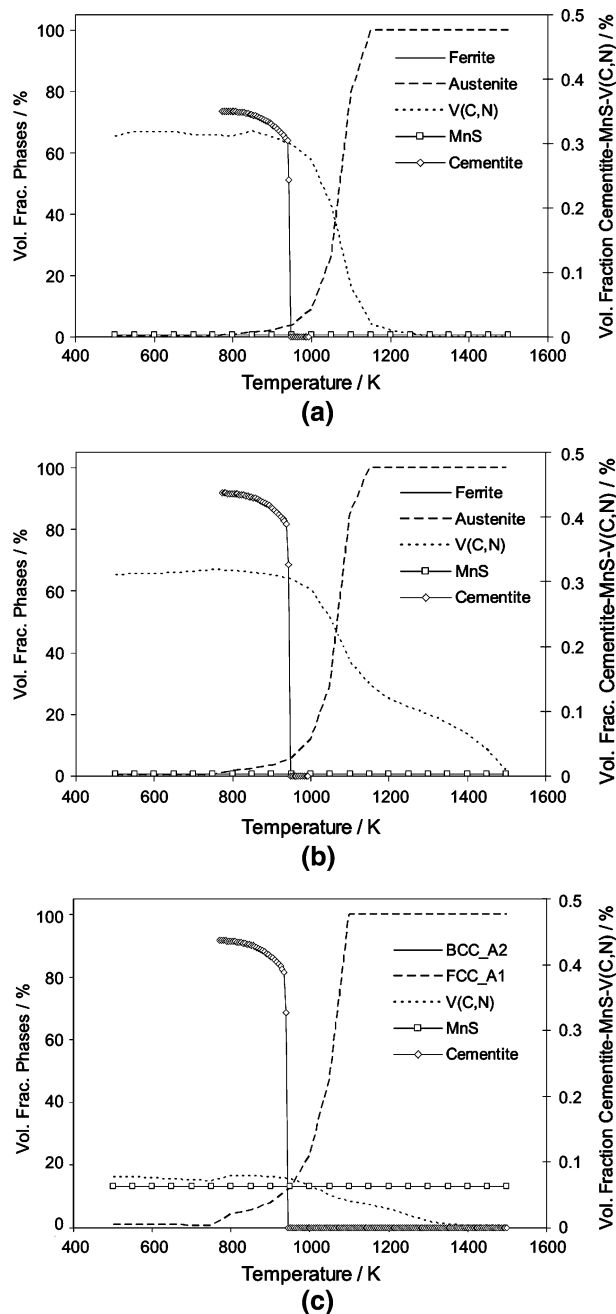


Fig. 15—Evolution of phases in (a) 4B, (b) 5B, and (c) 12P steels.

to be the actual trend observed in this study. The values of the crystallographic packet size (d) measured from Figure 5 (values of 3.5 and 10 μm for 5B and 4B steels, respectively) reveal a significantly lower d value for 5B steel than for 4B steel. Moreover, these d values are consistent with the smaller size in cleavage facets observed in 5B steel (Figure 7(b)) as compared to 4B steel (Figure 7(a)). Therefore, the crystallographic packet size values (among the micrographs shown in Figure 3) confirm that 4B steel has a microstructure coarser than that of 5B steel. Hence, 5B steel would be expected to have a lower DBT temperature; remarkably, however, both steels have similar DBT temperatures.

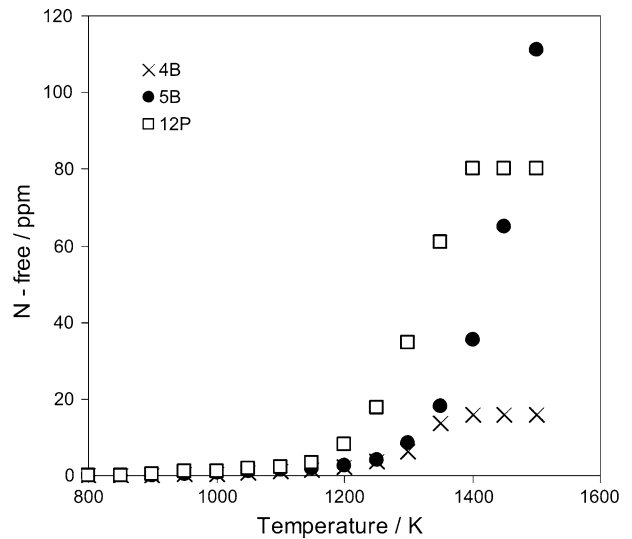


Fig. 16—Evolution of free nitrogen in 4B, 5B, and 12P steels.

The fractographic analysis at the DBT temperature revealed that the crack initiation site is not related to inclusions or particles but to grain boundaries, in both 4B (Figures 9 and 10) and 5B steels (Figures 8 and 11), regardless of the TC temperature tested. This pattern was also observed at -196°C (Figure 7). By contrast, the crack initiation in 12P steel (Figures 12 and 13 for TCs of 630°C and 550°C , respectively) is associated with inclusions. However, these results cannot explain the discrepancies between the DBT temperature and the effective grain size observed in 4B and 5B steels. Thus, it is clear that alternative explanations are required in order to understand the toughness results.

The similar values of the DBT temperatures of 4B and 5B steels could be related to the high level of V(C,N) precipitates in 5B steel. However, the volume of precipitates in the austenite before transformation should be independent of the TC temperature. Therefore, this explanation was ruled out. An alternative explanation could be related to the higher N content of 5B steel. It has been argued that N makes low-carbon steels more brittle.^[36] The DBT temperature of the steels increases with an increase in the total N content.^[37] Likewise, the interstitial nitrogen atoms gather to the dislocations and cause the strain-aging embrittlement of the steels. Nevertheless, the MTDATA calculations shown in Figure 16 predict that no free N remains at room temperature, which is consistent with the absence of a yield-point elongation in the stress-strain curves of the tensile tests.

Finally, the reason for the similarity in the values of the DBT temperatures in 5B and 4B steels could be related to the amount of cementite precipitation. In this vein, it could be concluded from Figure 15 that, with an increasing N content, a higher amount of V is tied up. Thus, a lower amount of V will combine with carbon to form V carbides. Hence, the excess of carbon in 5B steel as compared to 4B and 12P steels will trigger the interlath cementite precipitation, as is shown in Figure 17. Cementite laths are precipitated in the

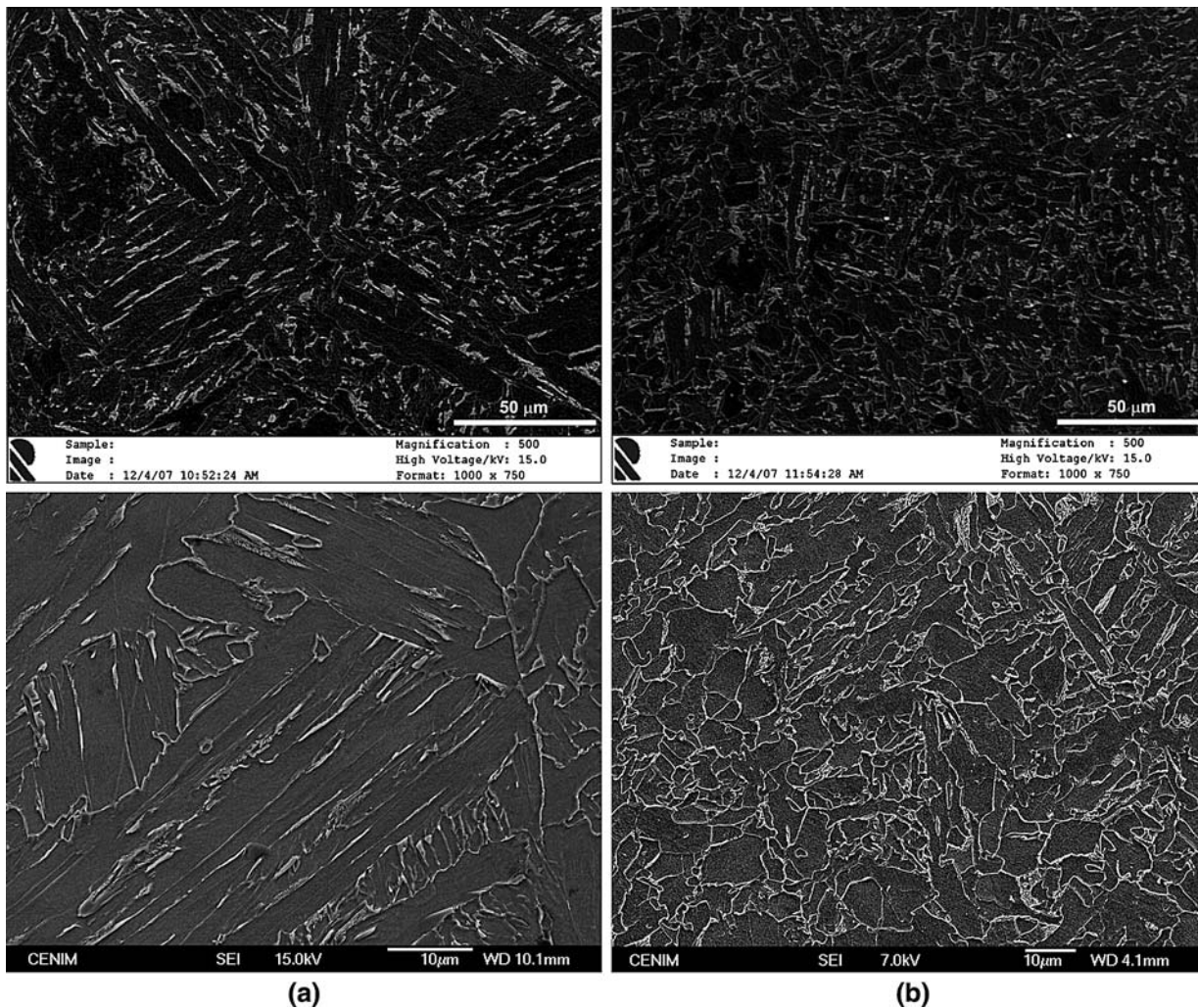


Fig. 17—FEG-SEM image showing cementite precipitation as light gray platelets on ferrite interlath in (a) 4B and (b) 5B steels after TC of 630 °C.

boundary between the ferrite plate and austenite during the growth of acicular ferrite plates (Figure 18). As transformation proceeds, carbon is depleted from the ferrite plate to austenite and the carbon coming from adjacent ferrite plate is accumulated into the untransformed austenite; once it is saturated in carbon cementite, precipitation occurs. Moreover, the carbon that does not diffuse away from the ferrite is trapped inside and promotes a second precipitation process in the form of very fine precipitates (likely to be vanadium carbides) inside the ferrite plates, as is seen in Figure 18.

Moreover, as was mentioned earlier, the coarser cementite present at a TC of 630 °C will shift the DBT temperature to higher values than is the case for a TC of 550 °C, at which temperature cementite is considerably finer.

V. CONCLUSIONS

The following conclusions can be drawn from this study.

1. Two S-lean laboratory heats and different N additions (5B steel for a high N content and 4B for a low N content) have been studied and compared with an industrial heat (12P steel). The FEG-SEM observations revealed that V precipitates act as nucleation sites for acicular ferrite in the absence of sulfide inclusions.
2. The microstructural analysis revealed that VN precipitation seems to lead to a coarse acicular ferrite structure, whereas VC leads to a lathlike bainitic structure.
3. The 5B steel presents higher YS and UTS values than the 4B and 12P steels, without a significant decrease in elongation. Thus, 5B steel presents the best combination of strength and ductility of the steels tested.
4. The higher energy value of the upper shelf of 4B as compared to 5B steel can be explained on the basis of the lower YS value. The variations in the upper-shelf energy values of 5B steel with the TC temperature is strongly related to the precipitation of coarse cementite. Moreover, the expected increase in the

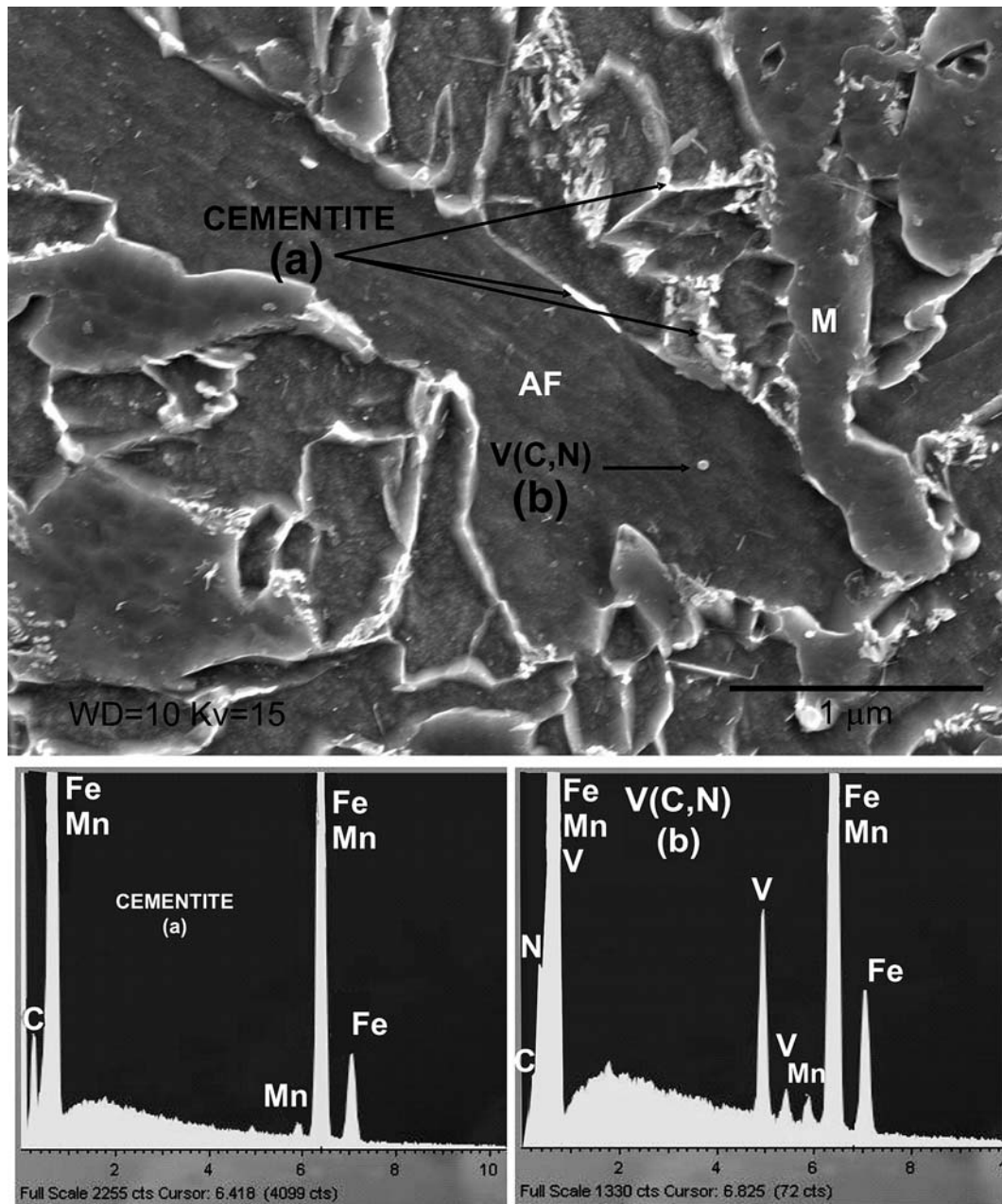


Fig. 18—Cementite plates between ferrite laths in 5B steel.

absorbed energy of 12P steel is offset by the higher inclusion content, regardless of the TC studied.

5. In addition to the smaller effective grain size for 5B than for 4B steel, similar transition temperatures for both steels have been recorded for a TC of 630 °C. This fact is strongly related to the amount of cementite precipitated between ferrite laths, which is higher in 5B than in 4B steel.
6. The DBT temperature is decreased in 5B steel as the TC is lowered, because cementite particles finer than those obtained at a TC of 630 °C are formed. By contrast, no change in the DBT temperature has been detected in 4B steels, because the microstructure

obtained after a TC of 550 °C presents a bimodal distribution in grain size and the coarse grain size controls the cleavage fracture. In regard to the 12P steel, because the cleavage fracture is controlled by the inclusion content, no changes in the DBT temperature with a decreasing TC temperature have been detected.

7. Finally, and most significantly, an acicular ferrite steel with a large volume of vanadium and nitrogen and the absence of sulfur in the chemical composition (5B steel) matches the toughness properties of a bainitic steel (4B steel) with a considerably lower amount of nitrogen, but substantially improves the YS and UTS properties.

ACKNOWLEDGMENTS

The authors acknowledge the Commission of the European Communities for its financial support within the framework of the RFCS Programme for 2004 (RFS-PR-03136). The authors also acknowledge their project partners: PROFILARBED (ProfilARBED, Mittal Steel Group, Differdange, Luxembourg), CRM (Centre Recherches Metallurgiques, Gent, Belgium), KIMAB (Swerea KIMAB AB, Stockholm, Sweden), and SZMF (Salzgitter Mannesmann Forschung GmbH, Duisburg, Germany). The authors also express their gratitude for the financial support of the Spanish Ministerio de Educación y Ciencia (MEC) through Project MAT2005-24485-E.

REFERENCES

1. Y.E. Smith, A.P. Coldren, and R.L. Cryderman: *Toward Improved Ductility and Toughness*, Climax Molybdenum, Tokyo, 1972, pp. 119–42.
2. S.S. Babu: *Curr. Opin. Solid State Mater. Sci.*, 2004, vol. 8, pp. 267–78.
3. S.S. Babu and H.K.D.H. Bhadeshia: *Mater. Trans., JIM*, 1991, vol. 32, pp. 679–88.
4. I. Madariaga, I. Gutierrez, and H.K.D.H. Bhadeshia: *Metall. Mater. Trans. A*, 2001, vol. 32A, pp. 2187–97.
5. M. Strangwood and H.K.D.H. Bhadeshia: *Advances in Welding Science and Technology*, ASM, Metals Park, OH, 1987, pp. 209–13.
6. M.C. Zhao, Y.Y. Shan, F.R. Xiao, and K. Yang: *Mater. Sci. Technol.*, 2003, vol. 19, pp. 355–59.
7. I. Madariaga, I. Gutierrez, C. Garcia-de Andres, and C. Capdevila: *Scripta Mater.*, 1999, vol. 41, pp. 229–35.
8. C. Capdevila, F.G. Caballero, and C. Garcia de Andres: *Metall. Mater. Trans. A*, 2001, vol. 32A, pp. 1591–97.
9. C. Capdevila, F.G. Caballero, and C. Garcia de Andres: *ISIJ Int.*, 2001, vol. 41, pp. 1083–92.
10. C. Capdevila, J.P. Ferrer, C. Garcia-Mateo, F.G. Caballero, V. Lopez, and C. Garcia de Andres: *ISIJ Int.*, 2006, vol. 46, pp. 1093–1100.
11. M.G. Hall and H.I. Aaronson: *Metall. Mater. Trans. A*, 1994, vol. 25A, pp. 1923–31.
12. R.A. Ricks, P.R. Howell, and G.S. Barrite: *J. Mater. Sci.*, 1982, vol. 17, pp. 732–40.
13. J.M. Gregg and H.K.D.H. Bhadeshia: *Acta Mater.*, 1997, vol. 45, pp. 739–48.
14. K. Yamamoto, T. Hasegawa, and J. Takamura: *ISIJ Int.*, 1996, vol. 36, pp. 80–86.
15. H. Mabuchi, R. Uemori, and M. Fujioka: *ISIJ Int.*, 1996, vol. 36, pp. 1406–12.
16. J.-L. Lee and Y.-T. Pan: *ISIJ Int.*, 1995, vol. 35, pp. 1027–33.
17. Z. Zhang and R.A. Farrar: *Mater. Sci. Technol.*, 1996, vol. 12, pp. 237–60.
18. J.-L. Lee and Y.-T. Pan: *Mater. Sci. Technol.*, 1992, vol. 8, pp. 236–44.
19. Z.H. Guo, T. Furuhashi, and T. Maki: *Scripta Mater.*, 2001, vol. 45, pp. 525–32.
20. F. Ishikawa, T. Takahashi, and T. Ochi: *Metall. Mater. Trans. A*, 1994, vol. 25A, pp. 929–36.
21. T. Furuhashi and T. Maki: *Mater. Sci. Eng., A*, 2001, vol. A312, pp. 145–54.
22. I. Madariaga and I. Gutierrez: *Acta Mater.*, 1999, vol. 47, pp. 951–60.
23. C. Garcia-Mateo, C. Capdevila, F.G. Caballero, and C. Garcia de Andres: *ISIJ Int.*, 2008, vol. 48, pp. 1270–75.
24. C. Garcia-Mateo, J. Cornide, C. Capdevila, F.G. Caballero, and C. Garcia de Andres: *ISIJ Int.*, 2008, vol. 48, pp. 1276–79.
25. F.G. Caballero, C. Capdevila, and C.G. de Andres: *Mater. Sci. Technol.*, 2001, vol. 17, pp. 1114–18.
26. C. Capdevila, C.G. de Andres, and F.G. Caballero: *Scripta Mater.*, 2001, vol. 44, pp. 129–34.
27. “ASTM E-399 Standard Test Method for Plane Strain Toughness of Metallic Materials,” *Annual Book of ASTM Standards*, ASTM International, West Conshohocken, PA, 1995, vol. 03.01, pp. 412–42.
28. A. Pineau: in *Advances in Fracture Research ICF5*, D. Francois, ed., Pergamon Press, Oxford, United Kingdom, 1982, pp. 553–77.
29. A.C. Mackenzie, J.W. Hancock, and D.K. Brown: *Eng. Fract. Mech.*, 1977, vol. 9, pp. 167–88.
30. J.C. Lautridou and A. Pineau: *Eng. Fract. Mech.*, 1981, vol. 15, pp. 55–71.
31. G.R. Speich and W.A. Spitzing: *Metall. Trans. A*, 1982, vol. 13A, pp. 2239–58.
32. G.T. Hahn: *Metall. Trans. A*, 1984, vol. 15A, pp. 947–59.
33. A.F. Gourgues-Lorenzon: *Int. Mater. Rev.*, 2007, vol. 52, pp. 65–128.
34. M.A. Linaza, J.L. Romero, J.M. Rodriguez-Ibabe, and J.J. Urcola: *Scripta Metall. Mater.*, 1995, vol. 32, pp. 395–400.
35. M. Diaz-Fuentes, A. Iza-Mendia, and I. Gutierrez: *Metall. Mater. Trans. A*, 2003, vol. 34A, pp. 2505–16.
36. T. Yamane, K. Hisayuki, Y. Kawazu, T. Takahashi, Y. Kimura, and S. Tsukuda: *J. Mater. Sci.*, 2002, vol. 37, pp. 3875–79.
37. K.S. Bang, C. Park, and S. Liu: *J. Mater. Sci.*, 2006, vol. 41, pp. 5994–6000.